# Enhanced Recovery of Oil Mixtures from Calcite Nanopores Facilitated by $CO_2$ Injection

Hongwei Zhang,[1] Shihao Wang,[2] Xin Wang,[1] and Rui Qiao[1,*]

[1] Department of Mechanical Engineering, Virginia Tech, Blacksburg, VA 24061, United States

[2] Chevron Technical Center, Chevron, Houston TX, 77002, United States

[*] To whom correspondence should be addressed. Email: ruiqiao@vt.edu

**Abstract.** Slow production, preferential recovery of light hydrocarbons, and low recovery factors are common challenges in oil production from unconventional reservoirs dominated by nanopores. Gas injection-based techniques such as $CO_2$ Huff-n-Puff have shown promise in addressing these challenges. However, a limited understanding of the recovery of oil mixtures at the nanopore scale hinders their effective optimization. Here, we use molecular dynamics simulations to study the recovery of oil mixture (C10+C19) from a single 4 nm-wide calcite dead-end pore, both with and without $CO_2$ injection. Without $CO_2$ injection, oil recovery is much faster than expected from oil vaporization and features an undesired selectivity, i.e., the preferential recovery of the lighter C10. With $CO_2$ injection, oil recovery is accelerated, and its selectivity toward C10 is greatly mitigated. These recovery behaviors are understood by analyzing the spatiotemporal evolution of the C10, C19, and $CO_2$ distributions in the calcite pore. In particular, we show that interfacial phenomena (e.g., the strong adsorption of oil and $CO_2$ on pore walls, their competition, and their modulation of transport behavior) and bulk phenomena (e.g., solubilization of oil by $CO_2$ in the middle portion of the pore) play a crucial role in determining the oil recovery rate and selectivity.

**Keywords:** Unconventional reservoirs; nanopores; enhanced oil recovery; gas injection; oil composition; selectivity.

# 1 Introduction

Shale and tight oil reservoirs with massive hydrocarbon storage have emerged as a frontier in the global energy landscape, and their exploration and exploitation have expanded significantly in recent decades.[1] However, the production from these unconventional reservoirs still faces many challenges. These reservoirs have low porosity, often dominated by nanoscale pores, resulting in extremely low permeability. Such low permeability causes a rapid decline in oil production during the primary depletion, and the oil recovery factor is below, if not far below, 7%.[2] To reduce the revenue loss associated with low oil recovery factors, many enhanced oil recovery (EOR) methods have been developed to increase oil recovery in unconventional oil reservoirs.[3, 4]

Among the proposed methods, EOR by gas injection has attracted significant attention. Typical choices of injected gases include light hydrocarbons (e.g., $CH_4$ and/or $C_2H_6$), $CO_2$, and $N_2$.[4] The gas injection-based EOR in unconventional reservoirs is often performed through the Huff-n-Puff process.[4-7] In the Huff cycle, gas is injected into the reservoir through the production well till the downhole pressure reaches a certain threshold. Then, the production well is shut during the soaking cycle. The injected gas will permeate fractures and nanopores in the reservoir. As the permeation proceeds, the gas may swell the oil and lower its viscosity, thus mobilizing it from the rock matrix to the more conductive fracture network. After the soaking step, the production well is reopened, and oil and some injected gas are produced in the Puff cycle.[7] Gas-based Huff-n-Puff has seen successful applications in many fields, although failed cases have also been reported.[3, 6, 8-10] To exploit the full potential of Huff-n-Puff, a comprehensive understanding of its underlying physics is needed.

The physical processes involved in gas-based Huff-n-Puff depend on the nature of the crude oil in unconventional reservoirs. Oils in these reservoirs contain hydrocarbons with a broad spectrum

of molecular weights, e.g., those from the Bakken play contain a significant mole fraction of C1 and C5 to C36.[11] Because these hydrocarbons interact differently with the injected gases, they have different solubility in them, and their relative mole fraction governs oil-gas mixture properties such as minimum miscibility pressure (MMP), viscosity, and diffusivity.[7, 12-15] Therefore, the recovery of hydrocarbons of various molecular weights from reservoirs and its enhancement by gas injection is expected to differ. Understanding the selective recovery of hydrocarbons is crucial to optimizing Huff-n-Puff operations in practice.

Experimental studies aiming at understanding selective oil recovery during Huff-n-Puff have emerged in recent years. In core-scale tests, Hawthorne *et al*. exposed rock samples to $CO_2$ and revealed that lighter hydrocarbons (C7 to C14) are recovered faster than the heavier hydrocarbons (>C20) from all samples.[16, 17] The results suggest that, during $CO_2$-EOR, crude oil does not move as a homogeneous phase; instead, substantial deposition of heavy hydrocarbons on pore walls in the sample can occur, and a strong selectivity of hydrocarbon recovery is expected.[16, 17] Through a series of experiments, they concluded that, in addition to higher diffusivity, the greater solubility of lighter hydrocarbon contributes to the selective recovery of different oil components.[18]

While the above studies revealed the importance of the *bulk behavior* of oil-gas mixtures in the selective recovery of hydrocarbons from unconventional reservoirs, other studies highlighted the importance of *interfacial behavior*. In core-scale studies, Zhu *et al*. evaluated the recovery of C10-C17 binary mixture through Niobrara shale samples and found that the recovery of C17 is lower than C10.[19] Such selectivity is significantly mitigated when $CO_2$ is introduced. These phenomena are understood by noting that, due to the prevalence of nanopores in shales, a significant fraction of oil can interact strongly with pore walls, and such fluid-wall interactions modulate oil recovery. Specifically, in the absence of $CO_2$, the heavier C17 molecules adsorb more strongly on the pore

walls, which retard their recovery and enables preferential C10 recovery. When $CO_2$ is introduced, as showed by equilibrium molecular dynamics (MD) simulations,[20] C17 molecules are displaced from the pore walls by $CO_2$ molecules, and thus the preferential recovery of C10 is suppressed.

Besides experimental studies, theoretical and computational studies can provide insight into the selective recovery of hydrocarbons from unconventional reservoirs, including when the recovery is aided by gas injection. In this regard, MD simulations are instrumental in probing how interfacial phenomena affect such recovery. MD simulations have been used to study the selective adsorption of hydrocarbon on pore walls[21-23] and the alteration of flow behaviors by adsorbed molecules,[24-28] although most available work focused on gaseous rather than liquid hydrocarbons. For example, the recovery of different hydrocarbons from dead-end pores[29] and through pore throat[30, 31] have been studied. These studies showed that the selective adsorption of different components on pore walls and the wall-mediated coupling between the transport of different hydrocarbons are key factors governing the selective recovery of shale gas of different molecular weights from shales.[29] In particular, Ho *et al*. concluded that the surface diffusion of adsorbed shale gas molecules is responsible for the selectivity between methane and ethane when a pore is narrower than 1.8 nm.[30] Guided by MD simulations, Wang *et al*. developed an analytical transport model for modeling the differential release of gas mixture from shale reservoirs.[31] Their model accounts for the selective adsorption of different gas species on pore walls, slippage flow, and surface diffusion on pore walls. The model predicts a differential release of multicomponent gas mixtures from shale and tight gas reservoirs, and its prediction has been validated against MD simulations of gas release through a single pore throat.[31]

The previous work has advanced the fundamental understanding of the selective recovery of hydrocarbon mixture from unconventional reservoirs. Nevertheless, there is a lack of systematic

study of the selective recovery of oil mixtures aided by gas injection. Indeed, many questions on such recovery remain open. For example, how are heavy and light hydrocarbons recovered? What are the roles of interfacial phenomena (e.g., adsorption and modulation of transport by fluid-wall interactions) in the selective recovery of oils with different molecular weights? Can $CO_2$ injection mitigate the preferential recovery of lighter hydrocarbons and what are the underlying mechanisms? Answering these questions will benefit from time-resolved data on the oil composition and distribution across nanopores during oil recovery, especially at the single-nanopore scale. Answering these questions will also help guide the introduction of nanoscale physics into oil recovery models beyond those considering mainly thermodynamic effects (e.g., equation of state models such as the nanoPVT).[32-34]

In this work, we use MD simulations to study the recovery of a C10-C19 binary mixture from a dead-end nanopore by $CO_2$ injection. The rest of this manuscript is organized as follows. Section 2 presents the MD systems and methods. Section 3 presents the recovery behaviors of C10 and C19 and the underlying spatiotemporal evolution of oil and $CO_2$ density inside the nanopore. The selective recoveries of C10 and C19 without and with $CO_2$ are compared, and their underlying mechanisms are elucidated. Finally, conclusions are drawn in Section 4.

## 2 Simulation System, Protocol, and Methods

**System for oil recovery.** Our MD system is designed to investigate the recovery of residual oil from a dead-end nanopore aided by gas injection. As shown in Fig. 1, the system consists of a slit-shaped calcite nanopore connected to a gas bath whose pressure is controlled by a piston. The pore width is 4 nm, consistent with the fact that nanopores are ubiquitous in shale oil reservoirs. The pore length is set to 30 nm so that the slender shape of nanopores in real shales is captured reasonably well. Initially, the nanopore is filled with a binary oil mixture, and the bath is filled

with gas. Crude oils have complicated compositions. Here, C10 and C19 are selected to represent crude oil's light and heavy components. The initial C10-to-C19 mole ratio inside the nanopore is set as 1.4: 1, close to that found in an unconventional Bakken Formation reservoir in the Williston Basin.[11] The gas bath is filled with $CO_2$ to probe the effect of $CO_2$ injection on selective oil recovery from the nanopore. As a reference, we consider the case in which the gas reservoir is empty. A vacuum is placed on the piston's right side.

The simulation box measures 100.00 nm, 2.93 nm, and 26.46 nm in the x, y, and z-directions, respectively. The system is periodic in all directions. The y-length of the simulation box is chosen to minimize the computational cost and avoid finite size effect. The recovery of C10 and C19 molecules from a nanopore is mainly controlled by their effective size pertinent to their movement, which can be characterized using their radius of gyration. From our simulation trajectories, the radius of gyration of C10 and C19 are ~0.37 and 0.60 nm, respectively. Since these values are

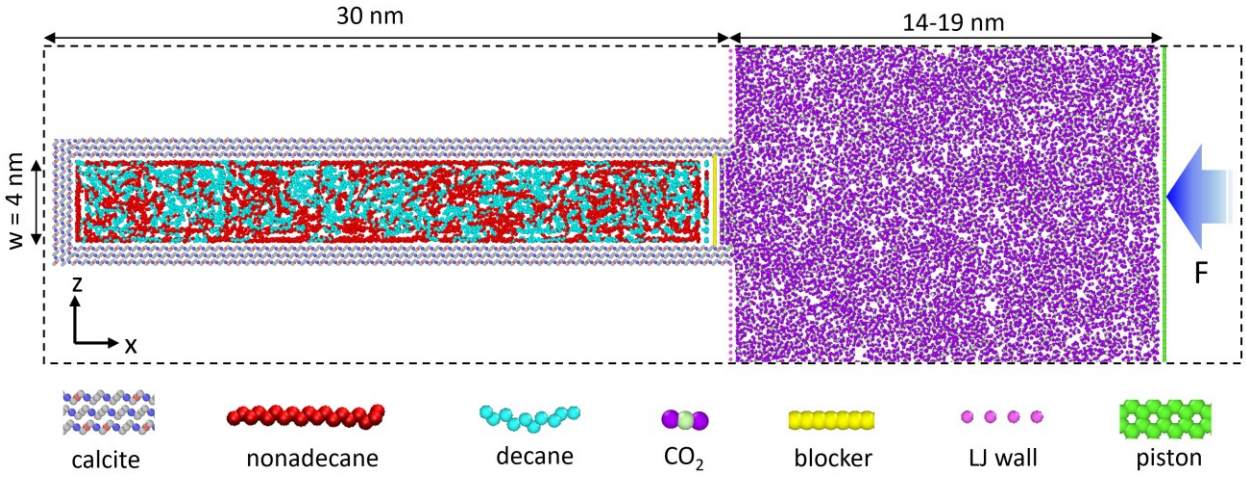


**Figure 1.** A snapshot of the simulation system for studying the recovery of decane+nonadecane (C10+C19) mixtures from a single calcite nanopore aided by $CO_2$ injection. The system measures 29.46 nm in the *z*-direction, and only part of the gas bath is shown to save space (see a full snapshot of the system in Fig. S1 of the Supporting Information). The dashed black lines denote the simulation box.

much smaller than the y-length of the simulation box (2.93 nm), the length of the simulation box in the y-direction should be adequate.

**Protocol for oil recovery study.** Before conducting the oil extraction simulation, separate simulations are first performed to determine the number of C10 and C19 molecules in the nanopore needed to produce the desired pressure (345 bar) and temperature (373K). Specifically, we set up a series of simulations in which the number of C10 molecules in the nanopore differed, but the mole ratio of C10 and C19 is kept at 1.4. In these simulations, blocker atoms in Fig. 1a are placed at the pore entrance, and the pressure on the blocker is measured. The system in which the pressure on the blocker matched the desired pressure (345 bar) is then selected. By trial and error, the number of C10 and C19 molecules in the nanopore is determined as 415 and 294, respectively.

Next, the nanopore is packed with C10 and C19 molecules determined above. Following this, $CO_2$ molecules are packed into the gas bath, and a constant force is applied to the piston to maintain a pressure of 345 bar (in the gas-free reservoir case, the piston is fixed in space). The system is equilibrated at 373 K for 5 ns.

After the above preparations, the blocker atoms in Fig. 1a are removed at t = 0, and a 240 ns production run is performed while the fluid temperature is maintained at 373 K. By the end of the production run, less than 2% of the initial C10 molecules remain inside the pore. Initially, the piston is ~19 nm from the pore entrance. As $CO_2$ enters the nanopore, the piston moves gradually toward the pore entrance and eventually reaches about 15 nm from the pore entrance at the end of the simulation. During the entire simulation, the piston is at least 15 nm away from the pore and vertical walls. This distance is far larger than the diameter (~0.4 nm) and the mean free path length of $CO_2$ molecules inside the gas bath (<1 nm). Therefore, a bulk behavior is always maintained inside the gas bath.

During each production run, any oil molecule reaching the gas bath is deleted. Furthermore, the pressure in the gas bath is maintained at 345 bar by applying a constant force on the piston. With these operations, the chemical potential of the gas inside the bath is maintained during the oil recovery process.

**Molecular models.** The 0.75 nm thick calcite pore wall is cut in the [1014] direction and fixed during simulations. The partial charges and LJ parameters of the calcite wall are from the re-fitted Doves' potential.[35] The NERD force field models the alkane molecules in this work with the $CH_3$ and $CH_2$ motifs treated as united atoms.[36] The force field for $CO_2$ molecules was developed by Zhu *et al*.[37] with parameters optimized by Wang *et al*.[38] These force fields are chosen based on their capabilities to describe the mixing and phase equilibrium behaviors of oil-$CO_2$ mixture accurately.[39] The piston and blocker atoms are modeled as Lennard-Jones (LJ) atoms arranged in a square lattice to prevent the oil and gas molecules from crossing them. The force field parameters used in this work can be found in Table. S1 in the Supporting Information. The Lorentz-Berthelot combination rule is applied to the interaction between other dissimilar atom pairs.

**Simulation methods.** All MD simulations in this study are performed using the LAMMPS code in the NVT ensemble (note that, under the action of the piston, the volume of the gas bath changes during the production run).[40] The temperature of the fluids is maintained at 373 K with a Nose-Hoover thermostat. The velocities of fluids in all three directions were thermostated because the collective velocity of the fluids in all directions (especially the x-direction) is small. The non-electrostatic interactions are computed with a cutoff length of 1.2 nm. Electrostatic interactions are handled using the PPPM, with a real-space cutoff length of 1.2 nm and an accuracy of $10^{-4}$. All simulations are conducted with a time step of 1 fs.

## 3 Results and Discussion

Before examining oil recovery from nanopores, let us first inspect the storage of the C10-C19 mixture in the pore at $t = 0$. Figure 2a shows the density profiles of C10 and C19 averaged along the pore length as a function of the distance from the lower pore wall (data in the upper half of the pore is not shown due to symmetry). Three layers of C10 and C19 molecules are identified near the pore wall. The first layers (< 0.53 nm) correspond to contact-adsorbed C10 and C19 molecules and are the most distinct. As shown in the side and top views of the system (see Fig. 2b and c), the adsorbed C10 and C19 molecules are highly stretched and prefer to adopt a co-planar structure on the wall. C19 adsorption is much stronger than C10 adsorption because, though the densities of the carbon atoms of C10 and C19 in the pore's bulk portion are comparable, the first C19 peak is

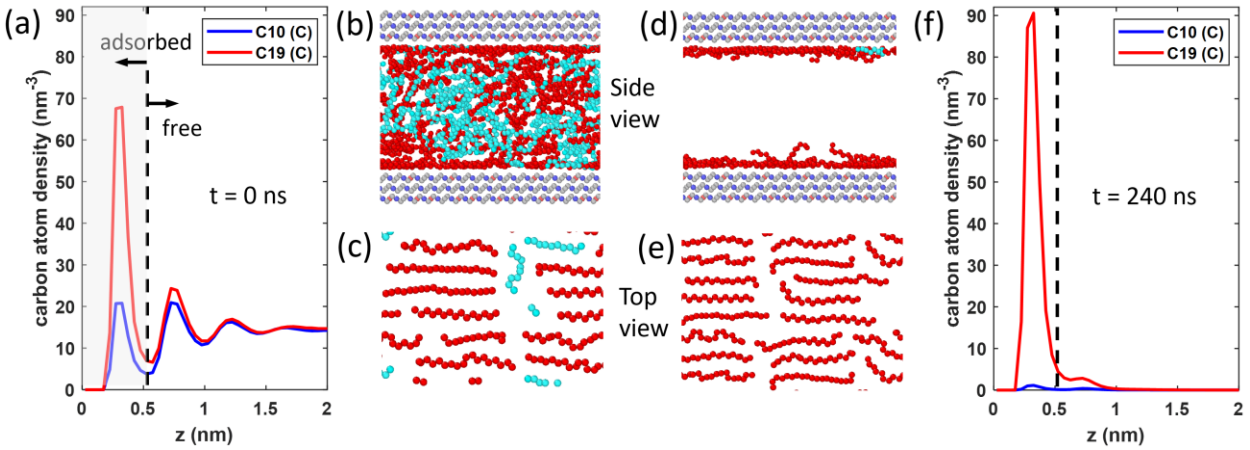


**Figure 2.** *Oil distributions in a calcite slit nanopore at the beginning and end of the oil recovery without gas injection*. (**a, f**) The density profiles of C10 and C19's carbon atoms across the pore at the simulation's beginning (a) and end (f). The density profiles are averaged along the entire nanopore and only shown in the lower half of the pore due to symmetry. (**b-e**) Snapshots of the representative side-view of the oil mixture inside the pore and top-view of the contact-adsorbed oil molecules at the beginning (b-c) and end (d-e) of the oil recovery simulation. In (a, f), $z = 0$ corresponds to the position of the uppermost oxygen atoms of the lower calcite wall.

more than 3 times higher than the first C10 peak. The stronger adsorption of C19 is attributed to its stronger van der Waals interactions with pore walls. Despite the stronger affinity of C19 to the pore wall, a modest amount of C10 is adsorbed on the pore wall. This is because, from an entropic perspective, the smaller C10 molecules do have an advantage for adsorption: it is easier for them to occupy the interstitial space on pore walls formed by the adsorbed C19 molecules (see Fig. 2c).

Given the distinct adsorption of C10 and C19 on pore walls, following convention,[13, 24, 30, 32, 34, 41] we divide each component in the pore into two populations: the "adsorbed" oil and the "free" oil (i.e., those behind and in front of the dashed line in Fig. 2a). As we will see later, from a transport perspective, the oil molecules in the second adsorption layer (z = 0.53-0.97 nm) are much more mobile than those in the first adsorption layer and relatively close to those of bulk oil. This is especially notable in the case without gas injection, where the molecules in the second layer mainly contribute to the oil recovery. Therefore, we define oil molecules beyond the first adsorption layer as "free" molecules. The adsorbed population account for 15.2% and 32.6% of all C10 and C19 inside the pore, respectively. As we shall see, the different fractions of the adsorbed population of C10 and C19 contribute significantly to their selective recovery from the pore.

### 3.1 Oil recovery without gas injection

In this reference case, there is no gas in the bath. Upon removing the blocker atoms at the pore entrance, driven by the pressure difference between the pore oil (345 bar) and the gas bath, the liquid oil mixture in the pore flows toward the bath and any C10/C19 molecules reached into the gas bath are deleted and considered recovered. However, given oil's low compressibility,[42] the pore pressure quickly relaxes, and the collective oil flow toward the gas bath diminishes. The recovery of oil from the pore is thus similar to the loss of oil trapped inside shale core samples exposed to a low-pressure environment. The present case is also relevant to the situation where condensates

are trapped in unconventional reservoirs during the final stage of the primary recovery,[41] when the pressure difference between the pore and fracture can no longer drive oil recovery.

The classical view of the present case is that oil is recovered via vaporization. Such a recovery is expected to be slow due to the low vapor pressure of the oil molecules considered here. Kinetic theories predict that the initial evaporation mass flux of oil species *i* is $J_i = \sqrt{m_i/2\pi RT}p_{sat,i}$, where T is the temperature. $m_i$, $R$, and $p_{sat,i}$ are the molecular mass, gas constant, and saturation pressure of an oil species *i*, respectively.[43] The vapor pressure of C10 and C19 mixtures is not readily available. Nevertheless, the order of magnitude of $J_{c10}$ and $J_{c19}$ can be estimated from the vapor pressure of neat C10 and C19 (9.5 kPa and 19 Pa)[44, 45] as 361 and 0.53 mol/m$^2$·s, respectively. If vaporization occurs across the entire opening of the nanopore, the initial recovery rates of C10 and C19 are estimated as 2.55 and 0.0037 molecules per nanosecond, respectively. As evaporation proceeds, the oil meniscus will recede into the pore, and the recovery rate will decrease due to the additional vapor transport resistance from the pore interior to the gas bath.

Figures 3a and 3b show the evolution of the number of C10 and C19 molecules inside the pore observed in our simulations. C10 is recovered at a faster rate than C19. At the end of the 240 ns simulations, 98.8% of the C10 molecules are recovered compared to 55.1% for C19. Equilibrium under the vacuum condition in the gas bath corresponds to the complete removal of C10 and C19 because of the tremendous entropic gain for transferring oil molecules into a vacuum, where oil concentration is zero (since oil molecules in the bath are removed during our simulations). Because our study focuses on the dynamics of oil recovery, and the oil recovery at t > 240 ns is extremely slow, reaching the equilibrium conditions in our simulations is unnecessary.

The initial recovery rates of C10 (C19) molecules are 8.92 $ns^{-1}$ (1.53 $nm^{-1}$), i.e., about one (three) orders of magnitude faster than that estimated above. The preferential recovery of C10 over C19 is maintained during the recovery process, indicating a strong selectivity toward lighter oil and the challenge of achieving a high recovery factor of heavy hydrocarbons in unconventional reservoirs. Such undesirable selectivity can be quantified using the selectivity factor, which is defined as the ratio between the fraction of C10 recovered and the fraction of C19 recovered. As shown in Fig. 3c, the selectivity factor decreases from an initial value of 3.0 to 1.8 at $t$ = 240 ns.

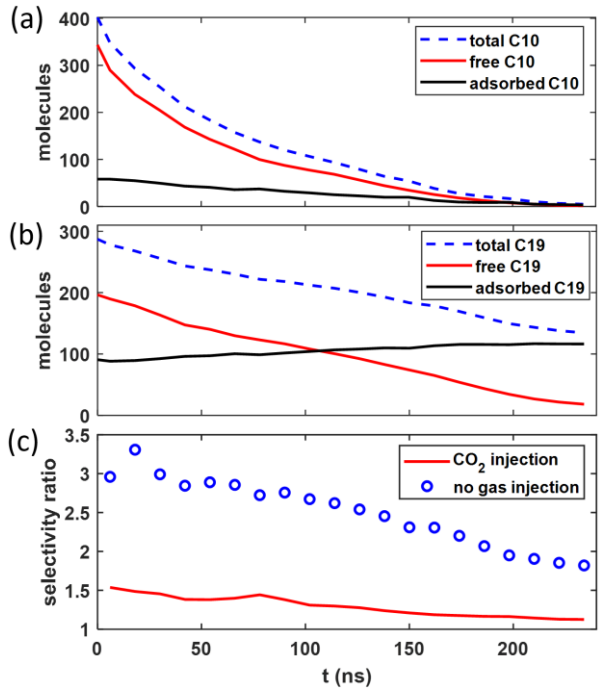


**Figure 3.** (**a-b**) The evolution of the number of C10 molecules (a) and C19 molecules (b) and their "free" and "adsorbed" as defined in Fig. 2a during oil recovery in the absence of gas injection. (**c**) The evolution of the selectivity ratio, i.e., the fraction of C10 recovered divided by the fraction of C19 recovered.

To understand the faster oil recovery compared to classical vaporization, we first visualize the recovery process. A representative snapshot of the system, taken at $t$ = 70 ns, is shown in Fig. 4a. As expected, a liquid meniscus (highlighted using a dashed line) has emerged and receded into the

pore. However, behind the meniscus, molecularly thin films of C10 and C19 appear on the pore walls. Oil molecules move mainly from the contact region between the liquid oil and pore walls into the thin liquid films, diffuse toward the pore opening, and are eventually recovered, which is akin to water imbibition into gas-filled nanopores through surface hydration and diffusion.[46] Further, the recovery of oil, especially the heavier C19 molecules, occurs mainly through the diffusion of oil molecules in the second adsorption layer due to their far higher mobility.

The transport of oil molecules along the liquid films behind the meniscus toward the gas bath helps explain the faster oil recovery than vaporization. To appreciate this, we compute the density profiles of C10 and C19 behind the meniscus at $t$ = 70 ns (i.e., in the region 17 nm < x < 30 nm, see the green box in Fig. 4a). The two density peaks of C10 in Fig. 4d correspond to the C10 adsorbed on each wall and the C10 adsorbed on top of the contact-adsorbed C10 molecules; similar observations apply to the C19 density profiles. Integration of these density profiles indicates that the amount of C10 and C19 molecules in these layers, if averaged across the pore width $w$, is 0.170 and 0.413 nm$^{-3}$, respectively (i.e., $\bar{\rho}_i = \int_0^w \rho_{c,i}(z)dz/w\, n_{c,i}$, where $\rho_{c,i}(z)$ is the number density of the carbon atoms of oil species $i$ shown in Fig. 4d. $n_{c,i} = 10$ (19) is the number of carbon atoms in each C10 (C19) molecule). Should oil recovery occur via vaporization only, the average density of C10 and C19 across the pore width would be estimated from their saturation vapor pressure to be on the order of $1.85 \times 10^{-3}$ and $3.72 \times 10^{-6}$ nm$^{-3}$, respectively. These data show that pore walls interacting strongly with oil molecules lead to their significant enrichment behind the meniscus moving toward the pore's interior, thus contributing to faster oil recovery than vaporization alone. The transport of oil molecules adsorbed on pore walls is slower than the oil molecules diffusing in the gas phase, but that appears to be a secondary effect here.

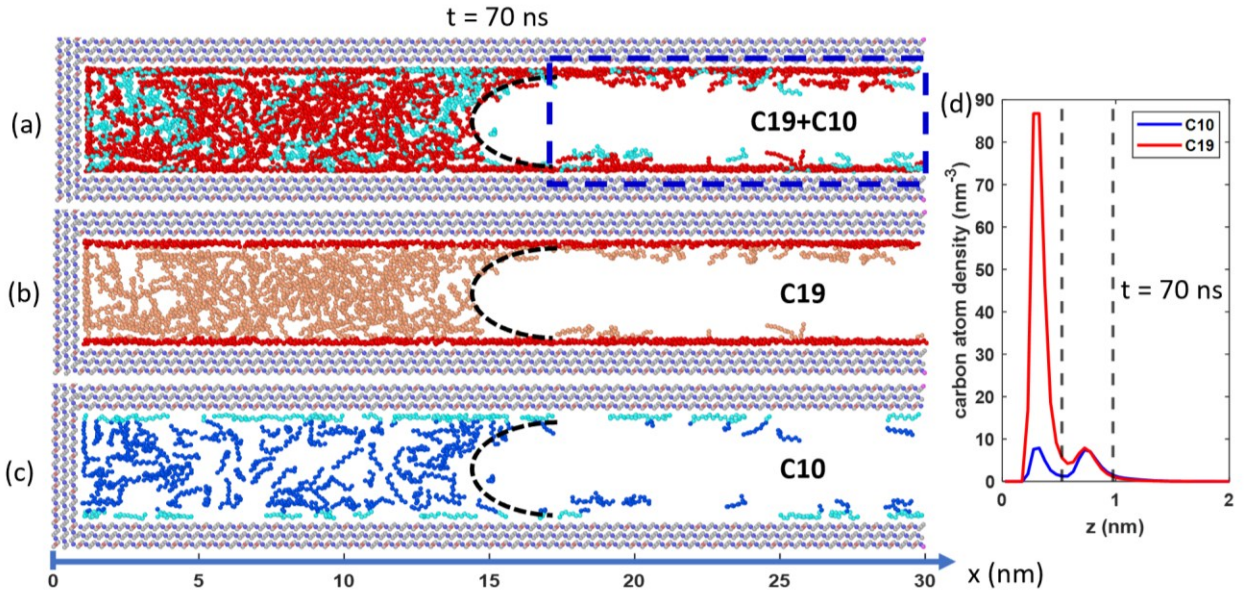


**Figure 4.** (**a-c**) Side-view snapshots of the calcite nanopore and oil inside it at $t$ = 70 ns of the oil recovery simulation under the no gas injection condition. The black dashed lines are guides for the liquid meniscus. The blue dashed box denotes the space behind the liquid meniscus. (**d**) The density profiles of C10 and C19 across the calcite pore averaged inside the green box in (a). In (b), red and light red denote the adsorbed and free C19 molecules. In (c), light blue and blue denote the adsorbed and free C10 molecules.

The selectivity of C10 over C19 during oil recovery assisted by surface adsorption has several origins. The recovery rate of each species through the liquid films behind the meniscus is governed by its amount inside the liquid films, the chemical potential gradient driving it toward the gas bath, and its mobility. The total amount of C19 inside the liquid films is higher than C10, e.g., at $t$ = 70 ns, there are 2.4 times more C19 than C10 molecules. However, our visualization of simulation trajectories reveals that C19 recovery is mainly contributed by molecules in the second adsorption layer (for C10 molecules, which occupy the interstitial space between contact adsorbed C19 and often straddle between the first and second adsorption layers, those in the first adsorption layer are recovered relatively readily, albeit more slowly than those in the second layer). Because C19 is

more enriched in the first adsorption layer than in the second adsorption layer (see Fig. 4b-c, which show C10 and C19 molecules separately and highlight the adsorbed molecules), the enrichment of C19 in the second adsorption layer is weaker than C10. In fact, integration of the second C10 and C19 peaks reveals that the number of C19 molecules in the second adsorption layer is only 0.63 times of C10 molecules there, compared to the C19:C10 ratio of 0.71 in the initial oil mixture. Therefore, the number of C19 molecules in the liquid films participating in oil recovery is smaller than those of C10, thus contributes to the observed selectivity of C10 over C19 during oil recovery. Furthermore, the longer chain of C19 molecules makes them less competitive in recovery than C10 through two other mechanisms: C19 molecules interact more strongly with their surrounding oil molecules and wall atoms, which leads to lower mobility and smaller chemical potential gradient driving their recovery.

Having studied the overall recovery behaviors of C10 and C19, we next examine how the two populations (free vs. adsorbed) of oil molecules are recovered from the nanopore. Figure 3a shows that the number of free and adsorbed C10 molecules decreases with time, but the reduction of free C10 dominates C10 recovery, given its larger population than adsorbed C10. The recovery of C19, shows a different picture: while the number of free C19 decreases with time and approaches zero, that of adsorbed C19 *increases* with time. The latter is consistent with the observation that the first C19 density peak at the end of the oil recovery simulation is higher than that at $t = 0$ (cf. Fig. 2a and Fig. 2f). During oil recovery, adsorbed C19 molecules leave the pore by surface diffusion. However, C19 molecules leaving the liquid meniscus easily become adsorbed on pore walls before leaving the pore. Further, free C19 molecules also move to vacant spots left by the C10 molecules departing the pore. During the period probed in our simulation, such replenishment of adsorbed C19 occurs faster than the depletion of adsorbed C19 from the pore, thus leading to an increase of

adsorbed C19. At $t$ = 240 ns, pore walls are still populated by C19 molecules that conform closely to them (see Fig. 2d-e). At a much larger time scale, adsorbed C19 molecules would be recovered, albeit at an even slower rate. In real reservoir operations, even though surface-enhanced recovery may help recover some heavy oil, fully recovering the oil contact adsorbed on pore walls is likely impractical.

### 3.2 Enhanced oil recovery with $CO_2$ injection

Figure 5 shows the evolution of the fraction of C10 and C19 recovered from the pore when the gas bath is filled with $CO_2$. Oil recovery is greatly accelerated by $CO_2$ injection: compared to the case in Section 3.1, for C10, the time for a 90% recovery has decreased from 161 ns to 107 ns; for C19, a 55.1% recovery is achieved at 73 ns instead of 240 ns. Further, the undesired selectivity of recovery is mitigated by $CO_2$ injection: as shown in Fig. 3c, the selectivity factor has been lowered to 1.5 initially and to 1.1 as time approaches 240 ns.

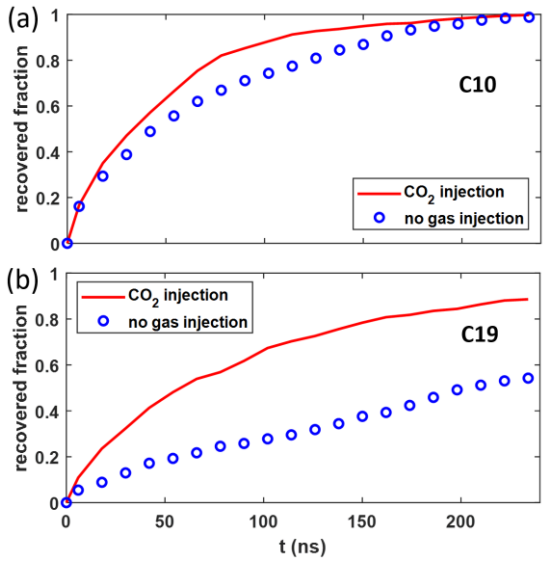


**Figure 5.** (**a-b**) The evolution of the fraction of C10 molecules (a) and C19 molecules (b) recovered during the oil recovery simulations performed with and without $CO_2$ injection.

We can qualitatively understand the acceleration of oil recovery and mitigation of the recovery selectivity by examining the molecular processes underlying these phenomena. Visualization of the trajectories reveals that, at $t > 0$, $CO_2$ molecules move toward the pore's interior in a diffusion-like mode (see Fig. S2 in the Supporting Information). The diffusion-like transport of $CO_2$ is similar to that reported in recent MD works.[24, 25, 47, 48] A representative snapshot of the system taken at $t = 25$ ns is shown in Fig. 6. A $CO_2$ diffusion front is observed at $x \approx 7$ nm. Near this diffusion front, where the $CO_2$ loading is low, $CO_2$ is mainly absorbed on pore walls. As we move from the diffusion front toward the pore opening, $CO_2$ loading increases, and $CO_2$ molecules are observed across the entire pore. $CO_2$ can displace C10 and C19 molecules from pore walls, especially in the region far behind the diffusion front. This is seen in Fig. 6c, where the average C10, C19, and $CO_2$ density across the pore behind the diffusion front (i.e., in the region 7 nm $< x <$ 30 nm) at $t = 25$ ns is shown. The more competitive adsorption of $CO_2$ on calcite pore walls is well known. It can be attributed to the electrostatic quadrupole-charge interactions between $CO_2$ molecules and the ionic sites on calcite surfaces.[24, 25, 27, 47, 49] The density peaks of $CO_2$ molecules are slightly closer to the wall than oil due to their smaller size along the minor axis compared to the alkane molecules.

C10 and C19 molecules displaced from pore walls enter the bulk portion of the pore, where $CO_2$ is mixed well with C10 and C19 molecules to serve as a solvent for them. This solubilization effect allows the oil molecules across the entire pore width to transport toward the pore opening to be recovered rather through than the adsorption layer on pore walls, as in Section 3.1. Consequently, oil recovery is accelerated. The bulk solubilization and elimination of adsorbed oils are more beneficial for C19 recovery because the recovery of C19 molecules is hindered more by surface adsorption in the no gas-injection scenario in Section 3.1. Consequently, the preferential recovery of C10 over C19 is mitigated, as shown in Fig. 3c.

We can gain more insight into the $CO_2$ EOR by examining the spatiotemporal evolution of $CO_2$, C10, and C19 in the pore and how the amount of adsorbed and free oil is reduced. Because $CO_2$ molecules adsorb strongly on pore walls (see Fig. 6c), we also divide them into the adsorbed (less than 0.38 nm from the pore wall) and free (more than 0.38 nm from the pore wall) populations.

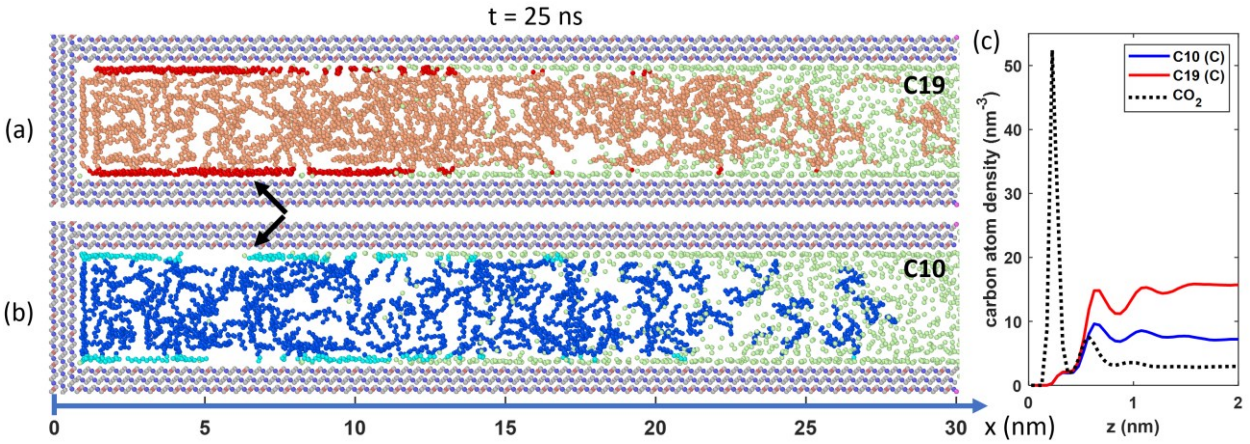


**Figure 6.** (**a-b**) Side-view snapshots of the calcite pore and fluids inside it at $t$ = 25 ns of the oil recovery simulation when the gas bath is filled with $CO_2$ at 345 bar. In (a), the red and light red denote the adsorbed and free C19 molecules. In (b), light blue and blue denote the adsorbed and free C10 molecules. The C atoms of $CO_2$ molecules are shown as green dots. The black arrow indicates the approximate location of the $CO_2$ diffusion front. (**c**) The density profiles of C10, C19, and $CO_2$ across the calcite pore averaged in the space behind the $CO_2$ diffusion front (7 nm < $x$ < 30nm) at $t$ = 25 ns.

During the early stage of oil recovery ($t$ < 25 ns), the $CO_2$ diffusion front moves rapidly toward the pore's dead end. A significant fraction of the $CO_2$ in the pore becomes adsorbed on pore walls due to their stronger affinity to pore walls than to bulk oil. The adsorbed $CO_2$ thus approaches its final state more rapidly than the free $CO_2$ (cf. Fig. 7a and 7b). By $t$ = 25 ns, the $CO_2$ diffusion front has reached ~ 7nm from the pore's end (see Fig. 6a), and the adsorbed $CO_2$ has reached 78.6% of its saturation value. The adsorbed $CO_2$ displaces adsorbed C10 and C19 off pore walls, which tends to elevate C10 and C19 densities in the pore's bulk portion. Indeed, a comparison of Figs. 2a and

8a shows that, despite that some C19 molecules are recovered from the pore by $t$ = 25 ns, the average C19 density in the pore's center at this time is *higher* than its initial value. While the $CO_2$ entering the pore solubilizes the oil and facilitates their recovery, as discussed above, Fig. 6a shows that the recovery factor of C10 only increases from 34.5% in the no gas injection case to 42.4% by $t$ = 25 ns. A more detailed look at the recovery of different oil populations (see Fig. 7c and 7d) reveals that, with $CO_2$ injection, by $t$ = 25 ns, 63.7% of adsorbed C10 has been removed from pore walls (compared to 9.2% in the no gas injection case), but the reduction of the free C10 inside the pore is nearly the same as in the no gas injection case.

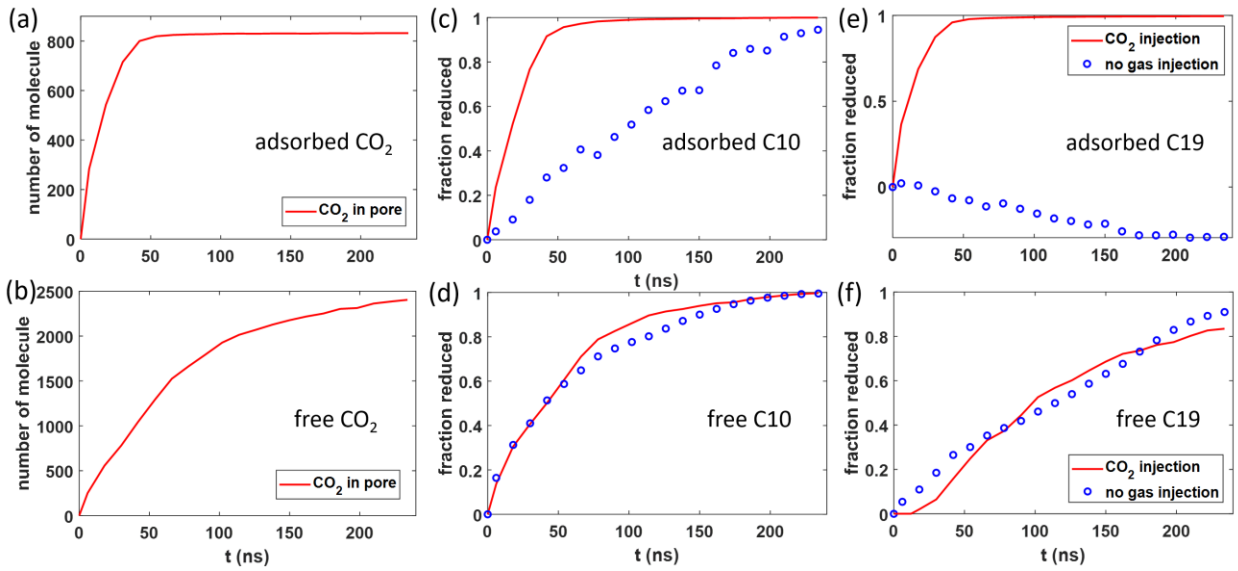


**Figure 7.** *Oil recovery in the presence of $CO_2$ injection*. (**a-b**) The evolution of the number of adsorbed (a) and free (b) $CO_2$ molecules inside the calcite pore. (**c-d**) The evolution of the reduction of the fraction of adsorbed (c) and free (d) C10 molecules inside the calcite pore during oil recovery. (**e-f**) The evolution of the reduction of the fraction of adsorbed (e) and free (f) C19 molecules inside the calcite pore during oil recovery.

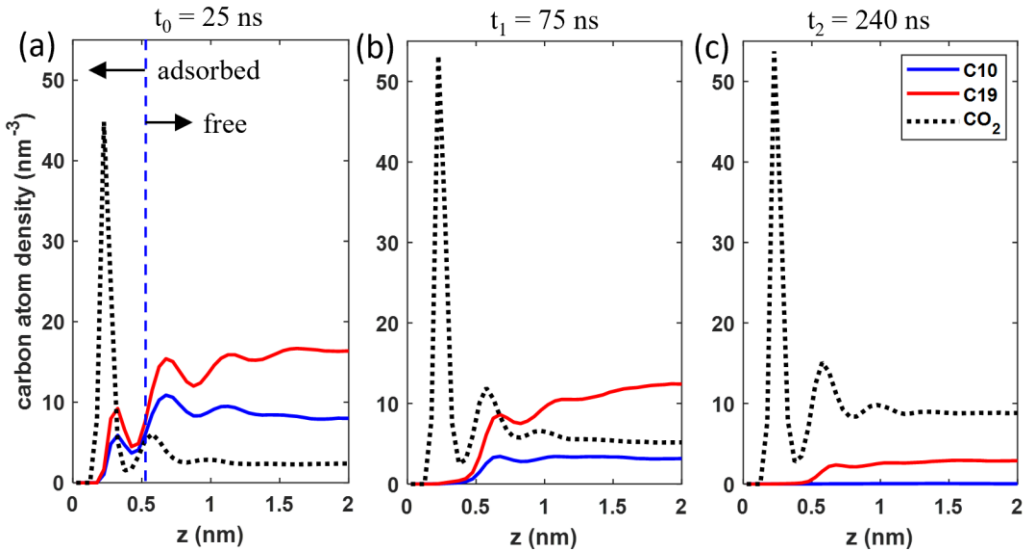


**Figure 8.** (**a-c**) The density profiles of C10, C19, and $CO_2$ across the calcite pore averaged inside the entire pore at t = 25 ns (a), 75 ns (b), and 240 ns (c).

To understand the marginal improvement of C10 recovery due to $CO_2$ injection at $t$ < 25 ns, recall that the flux of C10 inside a pore containing C10, C19, and $CO_2$ (denoted as species 1, 2, and 3) follows can be given by[29, 50-52] $J_1 = -\Gamma_{11}\nabla\mu_1 - \Gamma_{12}\nabla\mu_2 - \Gamma_{13}\nabla\mu_3$ according to non-equilibrium thermodynamics (here, the Onsager approach is preferred over the classical Fickian approach since it allows the coupling between the transport of different components to be more easily represented).[53, 54] Here, $\mu_i$ is the chemical potential of species $i$. $\Gamma_{ij}$ is the Onsager coefficient for species pair ($i$,$j$), which depends on the concentration of these species and their interactions. As can be expected from the limiting case of self-diffusion, $\Gamma_{ii}$ tends to increase as the mobility of species $i$ increases.[51]

In the no-gas injection case, C10 recovery is caused by the transport of the adsorbed C10 in the liquid films behind the meniscus, and thus the density of C10 transporting toward the pore opening is low. $CO_2$ allows C10 to be solubilized in the pore's bulk portion, which leads to an increased density of C10 transporting toward the gas bath. For example, at $t$ = 25 ns, the cross-section

averaged C10 density in the space behind the $CO_2$ diffusion front is 0.60 $nm^{-3}$, which is enhanced 3.53 times over the cross-section averaged density of 0.17 $nm^{-3}$ contributed by C10 in the liquid film behind the meniscus shown in Fig. 4c (if only C10 in the more mobile, second adsorption layer of the liquid films in Fig. 4c is considered, the enhancement factor is 6.0). Such an enhancement of C10 concentration helps increase $\Gamma_{11}$ and thus C10 transport out of the pore. However, two other factors tend to reduce C10 recovery. First, during the early stage of C10 recovery, the pore is characterized by a dispersion of $CO_2$ molecules in dense liquid oils. The interactions between C10 molecules and their surrounding C19 and $CO_2$ molecules tend to reduce C10's mobility, which tends to reduce $\Gamma_{11}$ and limit C10 recovery. Second, the ingression of $CO_2$ into the pore tends to drive C10 molecules toward the pore's dead end, thus suppressing their recovery. Given these two competing factors, the enhancement of C10 recovery by $CO_2$ injection becomes limited.

In sharp contrast to C10, the recovery of C19 during the early stage of oil recovery is enhanced significantly by $CO_2$ injection. Figure 5b shows that, at $t$ = 25 ns, the recovery of C19 has increased from 11.5% to 28.1% due to $CO_2$ injection. Figure 7e further reveals that 82.3% of the adsorbed C19 has been removed from the pore walls. Because a large portion of the displaced C19 molecules remains inside the pore as free C19, the total free C19 only reduces by 3.3% from its initial value (see Fig. 7f).

The accelerated recovery of C19 mainly originates from the significant increase of highly mobile C19 molecules that can be transported out of the pore. For example, at $t$ = 25 ns, the displacement of C19 molecules from pore walls to the pore's bulk portion leads to a cross-section averaged C19 density of 0.58 $nm^{-3}$ behind the $CO_2$ diffusion front. This density is almost 10 times of the cross-section averaged density of 0.06 $nm^{-3}$ contributed by the second C19 adsorption layer in the liquid

film behind the meniscus shown in Fig. 4c. Similar to C10 recovery, C19 recovery is also hampered by the dense molecular packing in oil-$CO_2$ mixture and the movement of $CO_2$ toward the pore's dead end. However, these factors appear far less important compared to the strong enhancement of C19 participating in the recovery process. Overall, the greater acceleration of C19 recovery than C10 at $t < 25$ ns reduces the selectivity factor from 3.0 in the no gas injection case to 1.5 when $CO_2$ is injected, as seen in Fig. 3c.

At $t \sim 30$ ns, the $CO_2$ diffusion front reaches the pore's dead end, and most of the adsorbed C10 and C19 molecules are removed from the pore walls by $t = 75$ ns. The average density profiles in Fig. 8b show that the C10 and C19 molecules are now separated from pore walls by a dense $CO_2$ layer. From $t = 25$ ns to 75 ns, the recovery of C10 increases from 42.4% to 80.8%, considerably higher than when there is no gas injection. This better enhancement of C10 recovery than in the initial stage ($t < 25$ ns) can be attributed to the enhancement of C10 mobility as time increases. As shown in Fig. 8b, at $t = 75$ ns, $CO_2$ density inside the pore has exceeded that of C10 and reached about half of C19. Such a $CO_2$-oil mixture is much less viscous than that at $t = 25$ ns. Therefore, the mobility and thus recovery of C10 molecules increase markedly. The recovery of C19 likewise shows a great enhancement over the no gas injection case from $t = 25$ ns to 75 ns for a similar reason. Over this period, the selectivity factor reduces only marginally.

As the recovery process reaches $t = 240$ ns, all C10 molecules are removed, and only about 18% of free C19 remains inside the pore (see Figs. 7c-f). The latter leads to an overall recovery of 89% for C19, compared to 55% when there is no gas injection (see Fig. 5). At $t = 240$ ns, the oil and $CO_2$ density profiles shown in Fig. 8c suggest that pore essentially contains a dilute solution of C19 molecules in a gaseous $CO_2$. The entropic gain driving the transport of C19 from the pore to the gas bath thus becomes small, and further recovery of C19 is sluggish.

All above results are obtained for calcite nanopores of 4 nm width. The selective recovery of C10 and C19 mixtures will differ for different pore widths. As the pore width decreases, interfacial effects become stronger. For example, a larger portion of C19 in the pore will be adsorbed on pore walls, hindering their recovery. So, the selectivity of C10 over C19 likely will enhance in the absence of gas injection. However, because a more significant fraction of injected $CO_2$ will adsorb on pore walls to displace adsorbed C19, the mitigation of C10 selectivity should be more significant as pore width decreases. The opposite trend will likely occur as pore width increases. Studies on how pore size affects recovery selectivity should be pursued in the future to obtain a thorough understanding of the pore width effects.

## 4 Conclusions

In summary, using molecular dynamics simulations, the recovery of an oil mixture composed of C10 and C19 from a single, 4 nm-wide calcite pore is studied with and without $CO_2$ injection. A large fraction of oil molecules is initially stored in the pore as adsorbed molecules, especially for the heavier C19. In the absence of gas injection, oil is recovered at rates much higher than expected from the oil vaporization mechanism alone, and a strong preferential recovery of C10 is observed. Oil recovery occurs through the diffusion of oil from the liquid meniscus along the molecularly thin liquid films on pore walls to the bath. The strong oil-wall interactions lead to a high oil density on walls to facilitate recovery but also reduce the mobility of oil molecules directly adsorbed on pore walls to hinder oil recovery. The latter is especially important for the heavier C19, which manifests as a stronger selectivity toward the lighter C10 during recovery.

When $CO_2$ is injected under miscible conditions, oil recovery is significantly accelerated, and the recovery selectivity toward C10 is mitigated. $CO_2$ molecules entering the pore rapidly displace oil molecules adsorbed on pore walls, and the $CO_2$ remaining in the pore's bulk portion solubilizes

C10 and C19. The latter dramatically increases the number of mobile oil molecules participating in recovery compared to the no gas injection case, where oil transport is largely a surface phenomenon. The $CO_2$ solubilization mechanism thus contributes decisively to the enhanced oil recovery. Compared to C10, a larger fraction of C19 is adsorbed on pore walls initially and has lower mobility. Therefore, the enhancement of C19 recovery by the solubilization mechanism is more distinct than C10, leading to a reduced selectivity of C10 recovery compared to the no gas injection case.

The results from our simulations highlight the crucial role of interfacial phenomena (in particular, competitive adsorption of oil and gas molecules and modulation of molecular transport properties by adsorption) in oil recovery from nanopores. Fundamentally, these phenomena and their relative significance compared to bulk phenomena depend on a host of factors not explored here, e.g., pore width, chemical nature of pore walls (e.g., whether walls are made of kerogen or minerals such as quartz and mica), existence of connate water, and type of gas injected (e.g., $CO_2$, $CH_4$, $N_2$, …). For example, at low connate water saturation, water exists as liquid films on pore walls. These water films, being more polar than oil and $CO_2$, displace oil from the pore walls but cannot be displaced by injected $CO_2$. Therefore, the enhanced recovery of C19 over C10 due to the displacement of adsorbed C19 by $CO_2$ molecules will disappear, and the efficacy of $CO_2$ injection in mitigating the preferential recovery of C10 over C19 may decrease. Further pore-scale MD simulations are warranted to explore how these factors affect the interfacial phenomena revealed here.

Ultimately, for pore-scale MD studies to benefit gas injection-based EOR at the reservior scale, it is helpful to combine MD studies with analytical and numerical models at larger scales (e.g., lattice Boltzmann or pore network models). Here, MD results can guide the development of analytical models, furnish thermodynamic and transport properties needed by those models, and serve as benchmarks

for testing their performance. It is encouraging that these aspects have already received attention in the literature.[55, 56]

## Supporting Information

Full snapshot of the simulation system; side-view snapshots of the fluids inside the calcite pore at different times with $CO_2$ in the gas bath; force field parameters for all molecules.

## Acknowledgments

The authors thank the ARC at Virginia Tech for the generous allocation of computing time and acknowledge the support from NSF under grant number CBET-2246274.

## References

(1) Energy Information Administration, Annual Energy Outlook 2022. U.S. Department of Energy, Washington, DC. **2022**, pp 28-30

(2) Clark, A. J. Determination of Recovery Factor in the Bakken Formation, Mountrail County, ND. In SPE Annual Technical Conference and Exhibition **2009**, SPE-133719-STU

(3) Sheng, J. J., Critical review of field EOR projects in shale and tight reservoirs. Journal of Petroleum Science and Engineering **2017**, 159, 654-665

(4) Wang, L.; Tian, Y.; Yu, X.; Wang, C.; Yao, B.; Wang, S.; Winterfeld, P. H.; Wang, X.; Yang, Z.; Wang, Y.; et al., Advances in improved/enhanced oil recovery technologies for tight and shale reservoirs. Fuel **2017**, 210, 425-445

(5) Abedini, A.; Torabi, F., On the CO2 storage potential of cyclic CO2 injection process for enhanced oil recovery. Fuel **2014**, 124, 14-27

(6) Zhou, X.; Yuan, Q.; Peng, X.; Zeng, F.; Zhang, L., A critical review of the CO2 huff ‘n’ puff process for enhanced heavy oil recovery. Fuel **2018**, 215, 813-824

(7) Jia, B.; Tsau, J.-S.; Barati, R., A review of the current progress of CO2 injection EOR and carbon storage in shale oil reservoirs. Fuel **2019**, 236, 404-427

(8) Rassenfoss, S., Shale EOR Works, But Will It Make a Difference? Journal of Petroleum Technology **2017**, 69 (10), 34-40

(9) Sheng, J. J., Enhanced oil recovery in shale reservoirs by gas injection. Journal of Natural Gas Science and Engineering **2015**, 22, 252-259

(10) Todd, H. B.; Evans, J. G. Improved Oil Recovery IOR Pilot Projects in the Bakken Formation. In SPE Low Perm Symposium **2016**, SPE-180270-MS

(11) Hawthorne, S. B.; Miller, D. J.; Jin, L.; Gorecki, C. D., Rapid and Simple Capillary-Rise/Vanishing Interfacial Tension Method To Determine Crude Oil Minimum Miscibility Pressure: Pure and Mixed CO2, Methane, and Ethane. Energy & Fuels **2016**, 30 (8), 6365-6372

(12) Li, C.; Pu, H.; Zhong, X.; Li, Y.; Zhao, J. X., Interfacial interactions between Bakken crude oil and injected gases at reservoir temperature: A molecular dynamics simulation study. Fuel **2020**, 276, 118058

(13) Zhang, L.; Liu, C.; Liu, Y.; Li, Q.; Cheng, Q.; Cai, S., Transport Property of Methane and Ethane in K-Illite Nanopores of Shale: Insights from Molecular Dynamic Simulations. Energy & Fuels **2020**, 34 (2), 1710-1719

(14) Vasileiadis, M.; Peristeras, L. D.; Papavasileiou, K. D.; Economou, I. G., Transport Properties of Shale Gas in Relation to Kerogen Porosity. The Journal of Physical Chemistry C **2018**, 122 (11), 6166-6177

(15) Collell, J.; Galliero, G.; Vermorel, R.; Ungerer, P.; Yiannourakou, M.; Montel, F.; Pujol, M., Transport of Multicomponent Hydrocarbon Mixtures in Shale Organic Matter by Molecular Simulations. The Journal of Physical Chemistry C **2015**, 119 (39), 22587-22595

(16) Hawthorne, S. B.; Miller, D. J.; Jin, L.; Azzolina, N. A.; Hamling, J. A.; Gorecki, C. D., Lab and Reservoir Study of Produced Hydrocarbon Molecular Weight Selectivity during CO2 Enhanced Oil Recovery. Energy & Fuels **2018**, 32 (9), 9070-9080

(17) Hawthorne, S. B.; Miller, D. J.; Grabanski, C. B.; Azzolina, N.; Kurz, B. A.; Ardakani, O. H.; Smith, S. A.; Sanei, H.; Sorensen, J. A., Hydrocarbon Recovery from Williston Basin Shale and Mudrock Cores with Supercritical CO2: Part 1. Method Validation and Recoveries from Cores Collected across the Basin. Energy & Fuels **2019**, 33 (8), 6857-6866

(18) Hawthorne, S. B.; Grabanski, C. B.; Miller, D. J.; Kurz, B. A.; Sorensen, J. A., Hydrocarbon Recovery from Williston Basin Shale and Mudrock Cores with Supercritical CO2: 2. Mechanisms That Control Oil Recovery Rates and CO2 Permeation. Energy & Fuels **2019**, 33 (8), 6867-6877

(19) Zhu, Z.; Fang, C.; Qiao, R.; Yin, X.; Ozkan, E. Experimental and Molecular Insights on Sieving of Hydrocarbon Mixtures in Niobrara Shale. In SPE/AAPG/SEG Unconventional Resources Technology Conference **2019**, D033S064R001

(20) Zhu, Z.; Fang, C.; Qiao, R.; Yin, X.; Ozkan, E., Experimental and Molecular Insights on Mitigation of Hydrocarbon Sieving in Niobrara Shale by CO2 Huff ‘n’ Puff. SPE Journal **2020**, 25 (04), 1803-1811

(21) Wang, S.; Yao, X. Y.; Feng, Q. H.; Javadpour, F.; Yang, Y. X.; Xue, Q. Z.; Li, X. F., Molecular insights into carbon dioxide enhanced multi-component shale gas recovery and its sequestration in realistic kerogen. Chemical Engineering Journal **2021**, 425, 130292

(22) Li, W.; Zhang, M.; Nan, Y.; Pang, W.; Jin, Z., Molecular Dynamics Study on CO2 Storage in Water-Filled Kerogen Nanopores in Shale Reservoirs: Effects of Kerogen Maturity and Pore Size. Langmuir **2021**, 37 (1), 542-552

(23) Liu, Y. L.; Ma, X. M.; Li, H. A.; Hou, J., Competitive adsorption behavior of hydrocarbon(s)/CO2 mixtures in a double-nanopore system using molecular simulations. Fuel 2019, 252, 612-621

(24) Moh, D. Y.; Zhang, H.; Wang, S.; Yin, X.; Qiao, R., Soaking in CO2 huff-n-puff: A single-nanopore scale study. Fuel **2022**, 308, 122026

(25) Moh, D.; Zhang, H. W.; Sun, S. Y.; Qiao, R., Molecular anatomy and macroscopic behavior of oil extraction from nanopores by CO2 and CH4. Fuel **2022**, 324, 124662

(26) Moh, D.; Fang, C.; Yin, X. L.; Qiao, R., Interfacial CO2-mediated nanoscale oil transport: from impediment to enhancement. Physical Chemistry Chemical Physics **2020**, 22 (40), 23057-23063

(27) Zhang, H.; Moh, D. Y.; Wang, S.; Qiao, R., Diffusio-osmosis of oil–CO<sub>2</sub> mixture in inorganic nanopores. Physics of Fluids **2022**, 34 (9), 092017

(28) Wu, H.; Chen, J.; Liu, H., Molecular Dynamics Simulations about Adsorption and Displacement of Methane in Carbon Nanochannels. The Journal of Physical Chemistry C **2015**, 119 (24), 13652-13657

(29) Wu, H.; He, Y.; Qiao, R., Recovery of Multicomponent Shale Gas from Single Nanopores. Energy & Fuels **2017**, 31 (8), 7932-7940

(30) Ho, T. A.; Wang, Y., Pore size effect on selective gas transport in shale nanopores. Journal of Natural Gas Science and Engineering **2020**, 83, 103543

(31) Wang, S.; Zhang, Y.; Wu, H.; Lee, S. H.; Qiao, R.; Wen, X.-H., A kinetic model for multicomponent gas transport in shale gas reservoirs and its applications. Physics of Fluids **2022**, 34 (8), 082002

(32) Travalloni, L.; Castier, M.; Tavares, F. W., Phase equilibrium of fluids confined in porous media from an extended Peng–Robinson equation of state. Fluid Phase Equilib. **2014**, 362, 335-341

(33) Luo, S.; Chen, F.; Zhou, D.; Nasrabadi, H., Multiscale Pressure/Volume/Temperature Simulation of Decreasing Condensate/Gas Ratio at Greater than Dewpoint Pressure in Shale Gas-Condensate Reservoirs. SPE Journal **2021**, 26 (06), 4174-4186

(34) Jin, B.; Li, L.; Sun, H.; Zhou, D. Hydrocarbon Phase Behavior Under Nanoconfinement and Shale-PVT Model Development. In SPE/AAPG/SEG Unconventional Resources Technology Conference, **2023**; URTEC: p D011S020R002.

(35) Rahaman, A.; Grassian, V. H.; Margulis, C. J., Dynamics of Water Adsorption onto a Calcite Surface as a Function of Relative Humidity. The Journal of Physical Chemistry C **2008**, 112 (6), 2109-2115

(36) Nath, S. K.; Escobedo, F. A.; De Pablo, J. J., On the simulation of vapor–liquid equilibria for alkanes. The Journal of Chemical Physics **1998**, 108 (23), 9905-9911

(37) Zhu, A.; Zhang, X.; Liu, Q.; Zhang, Q., A Fully Flexible Potential Model for Carbon Dioxide. Chinese Journal of Chemical Engineering **2009**, 17 (2), 268-272

(38) Peng, F.; Wang, R.; Guo, Z.; Feng, G., Molecular dynamics simulation to estimate minimum miscibility pressure for oil with pure and impure CO<sub>2</sub>. Journal of Physics Communications **2018**, 2 (11), 115028

(39) Wang, R.; Peng, F.; Song, K.; Feng, G.; Guo, Z., Molecular dynamics study of interfacial properties in CO2 enhanced oil recovery. Fluid Phase Equilib. **2018**, 467, 25-32

(40) Plimpton, S., Fast Parallel Algorithms for Short-Range Molecular Dynamics. Journal of Computational Physics **1995**, 117 (1), 1-19

(41) Wang, S.; Zhang, H.; Jin, B.; Qiao, R.; Wen, X.-H., Molecular insights of condensate trapping mechanism in shale oil reservoirs and its implications on lean gas enhanced oil recovery. Chemical Engineering Journal **2023**, 476, 146366

(42) Karnanda, W.; Benzagouta, M. S.; AlQuraishi, A.; Amro, M. M., Effect of temperature, pressure, salinity, and surfactant concentration on IFT for surfactant flooding optimization. Arabian Journal of Geosciences **2013**, 6 (9), 3535-3544

(43) Vaartstra, G.; Lu, Z.; Lienhard, J. H.; Wang, E. N., Revisiting the Schrage Equation for Kinetically Limited Evaporation and Condensation. Journal of Heat Transfer **2022**, 144 (8),

(44) Willingham, C. B.; Taylor, W. J.; Pignocco, J. M.; Rossini, F. D., VAPOR PRESSURES AND BOILING POINTS OF SOME PARAFFIN, ALKYLCYCLOPENTANE, ALKYLCYCLOHEXANE, AND ALKYLBENZENE HYDROCARBONS. Journal of Research of the National Bureau of Standards **1945**, 35 (3), 219-244

(45) Morecroft, D. W., Vapor Pressures of Some High Molecular Weight Hydrocarbons. Journal of Chemical & Engineering Data **1964**, 9 (4), 488-490

(46) Fang, C.; Qiao, R., Surface hydration drives rapid water imbibition into strongly hydrophilic nanopores. Physical Chemistry Chemical Physics **2017**, 19 (31), 20506-20512

(47) Peng, F.; Xiong, K.; Wang, R.; Li, Y.; Guo, Z.; Feng, G., Molecular Insight into Microbehaviors of n-Decane and CO2 in Mineral Nanopores. Energy & Fuels **2020**, 34 (3), 2925-2935

(48) Wang, R.; Bi, S.; Guo, Z.; Feng, G., Molecular insight into replacement dynamics of CO2 enhanced oil recovery in nanopores. Chemical Engineering Journal **2022**, 440, 135796

(49) Deng, X.; Zhang, Q.; Zhang, Z.; Li, Q.; Liu, X., Adsorption and diffusion behavior of CO2/H2 mixture in calcite slit pores: A molecular simulation study. J. Mol. Liq. **2022**, 346, 118306

(50) Krishna, R.; van Baten, J. M., An investigation of the characteristics of Maxwell–Stefan diffusivities of binary mixtures in silica nanopores. Chemical Engineering Science **2009**, 64 (5), 870-882

(51) Chempath, S.; Krishna, R.; Snurr, R. Q., Nonequilibrium Molecular Dynamics Simulations of Diffusion of Binary Mixtures Containing Short n-Alkanes in Faujasite. The Journal of Physical Chemistry B **2004**, 108 (35), 13481-13491

(52) Wang, Y.; LeVan, M. D., Mixture Diffusion in Nanoporous Adsorbents: Equivalence of Fickian and Maxwell−Stefan Approaches. The Journal of Physical Chemistry B **2008**, 112 (29), 8600-8604

(53) Hoteit, H., Modeling diffusion and gas–oil mass transfer in fractured reservoirs. Journal of Petroleum Science and Engineering **2013**, 105, 1-17

(54) Zhang, H.; Wang, X.; Kang, Q.; Yan, B.; Sun, S.; Qiao, R., Transport properties of oil-CO2 mixtures in calcite nanopores: Physics and machine learning models. Fuel **2024**, 358, 130308

(55) Yu, H.; Fan, J.; Xia, J.; Liu, H.; Wu, H., Multiscale gas transport behavior in heterogeneous shale matrix consisting of organic and inorganic nanopores. Journal of Natural Gas Science and Engineering **2020**, 75, 103139

(56) Yu, H.; Chen, J.; Zhu, Y.; Wang, F.; Wu, H., Multiscale transport mechanism of shale gas in micro/nano-pores. Int. J. Heat Mass Transf. **2017**, 111, 1172-1180

# TOC Image

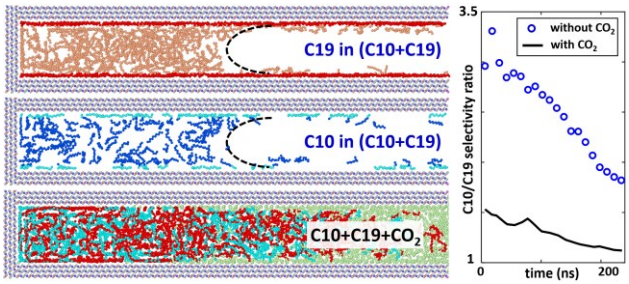
C19 in (C10+C19)
C10 in (C10+C19)
C10+C19+CO2
3.5
1
0
200
time (ns)
C10/C19 selectivity ratio
without CO2
with CO2